



Review

Post-buckling design of thin-film electrolytes in micro-solid oxide fuel cells



Yasser Safa ^{a,*}, Thomas Hocker ^a, Michel Prestat ^b, Anna Evans ^b

^a ICP Institute of Computational Physics, ZHAW Zurich University of Applied Sciences, Technikumstrasse 9, CH-8401 Winterthur, Switzerland

^b Nonmetallic Inorganic Materials, Department of Materials, ETH Zurich, Wolfgang-Pauli-Strasse 10, CH-8093 Zurich, Switzerland

HIGHLIGHTS

- Buckling analysis combined with experiments enabled to fabricate stable YSZ membranes.
- Effective residual stress in a free-standing YSZ film was estimated by a new method.
- Comparisons between simulations and experiments show excellent agreement.
- Novel post-buckling design space for thin electrolyte fabrication has been set up.

ARTICLE INFO

Article history:

Received 10 June 2013

Received in revised form

21 October 2013

Accepted 26 October 2013

Available online 6 December 2013

Keywords:

Microfabricated membrane

PLD

Film buckling

Energy method

Design space

ABSTRACT

The buckling behavior of a thin-film electrolyte of a micro-solid oxide fuel cell is investigated based on experimental measurements, analytical estimations and numerical simulations. An energy minimization procedure is applied in combination with the Rayleigh–Ritz method to represent the buckling modes, evaluate the buckling amplitude and determine the threshold values for instability transitions in the system. The residual stresses in the film deposited on a silicon substrate are evaluated based on wafer curvature whereby nanoindentations tests are applied to estimate the Young's modulus of the deposited film. The partial release of residual stresses in the film during free etching of the substrate is estimated by a new method combining pre-etching optical measurements with posteriori stress analysis. The energy interpretation of the obtained deflection shape is discussed. Comparisons between simulation results and experimental data show the efficiency of this method to predict various buckling stages of free-standing thin films. A post-buckling design space for thin-film electrolyte fabrication is presented by applying a stress-based failure criterion.

© 2013 Elsevier B.V. All rights reserved.

1. Introduction

Micro-solid oxide fuel cells (μ SOFC) are currently receiving increasing attention as promising electrochemical energy converter devices. The high conversion efficiency, the high power density, the fast start-up times and the low operational temperature (350–550 °C) make this a suitable power source for small portable electronic applications. Before reaching the promised potential of this technology, some challenges need to be overcome like, in particular, the thermomechanical stability during fabrication stages and under operational conditions. A μ SOFC is built of a multi-layered structure of ceramic and metallic plates. Although these structures exhibit advantageous properties such as a favorable strength-to-weight ratio, a high fatigue endurance, and a strong corrosion resistance, they may exhibit some functional problems.

For example, such a structure has a low resistance towards peeling stresses at the interface between different layers where delamination may occur. In addition, these films are subjected to in-plane stresses associated with both the thermal expansion mismatch and the fabrication process. This may induce either membrane buckling [1] under compression or membrane fracture under tension. Both buckling and cracks reduce the load carrying capacity of the structure [2]. Further, crack propagation can lead to complete failure limiting the operating time of the fuel cell.

The present work deals with the mechanical stress analysis and the design implications for the fabrication of thin films in μ SOFCs. The fabrication of μ SOFC membranes involves several steps of film deposition and layer etching as depicted in Fig. 1 (see Refs. [3] and [4]). After the etching of the silicon substrate (Fig. 1 (c)), the membranes are free-standing and the mechanical system in Fig. 1(g) is found to be a model of three-layer clamped plate which consists of: a top electrode, the electrolyte made of YSZ (as described in Ref. [3]) and a bottom electrode. The stability of such a system should be

* Corresponding author. Tel.: +41 58 934 77 22.

E-mail address: safa@zhaw.ch (Y. Safa).

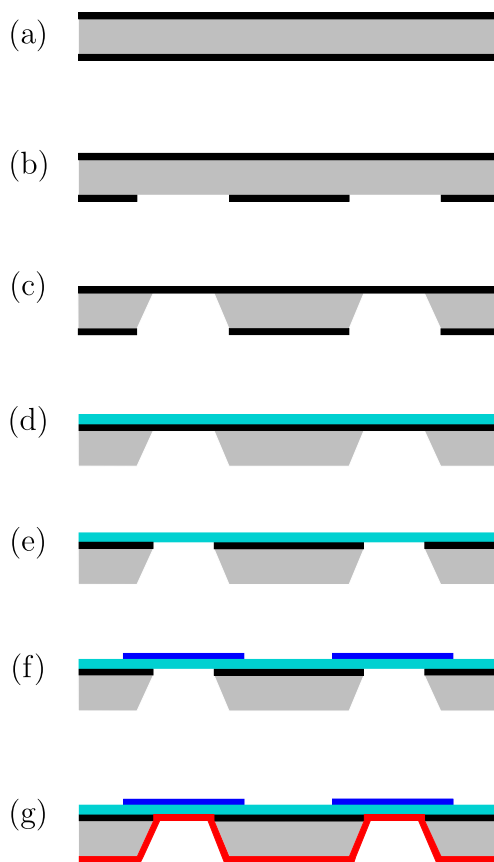


Fig. 1. The fabrication steps of μ SOFC membranes. (a) Silicon wafer double side coated with Si_3N_4 . (b) Backside photolithography, and reactive ion etching of Si_3N_4 (LPCVD). (c) Wet etching of Si in 20% aqueous KOH. (d) YSZ deposition by PLD onto free-standing Si_3N_4 membrane. (e) Reactive ion etching of Si_3N_4 membrane. (f) LSC Cathode deposition. (g) Anode deposition by platinum sputter-coating.

guaranteed under both fabrication and operation conditions at temperatures between 400 and 500 °C.

1.1. Design consideration for thin-film manufacturing

When PLD is employed, the deposited film exhibits different responses with respect to the deposition conditions and techniques. A high-temperature deposition may induce a residual compressive stress which drives the membranes to buckle. On the other hand, the deposition at room temperature may initiate, during a subsequent annealing up to 400 °C, cracks which propagate in the brittle film causing rupture under tensile stresses as shown in Fig. 3 (see also [3]). The residual stress is then a finger print of the deposition's mechanism type and the related conditions of temperature and pressure, see for example [5]. Another examples of the intrinsic effects are the phase transformation inside the film, the densification, the crystallization, and, the chemical association–dissociation which induces a strain, and subsequently, a chemomechanical stress in the material ([6] and [7]).

In this work, focus is made on the stress analysis and design of YSZ electrolyte fabricated by pulsed laser deposition PLD (see Fig. 1(e) and Fig. 2).

In the framework of μ SOFC, some design concepts are adopting a failure-based buckling criterion, like in Refs. [8], where the use of thick film is recommended to avoid both buckling and fracture. Such a design option suffers from drawbacks which are related to

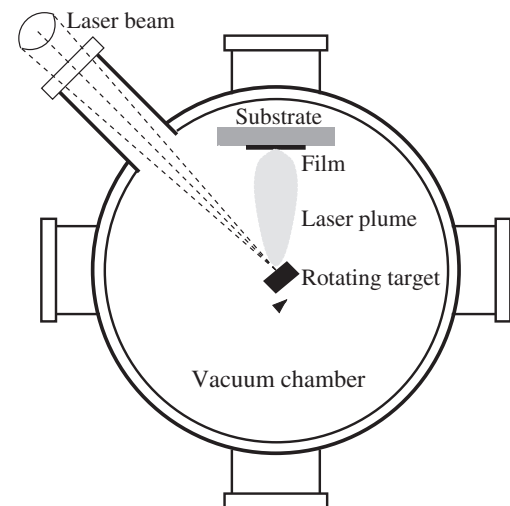


Fig. 2. Schematic representation of PLD techniques used in the fabrication of thin YSZ film deposited onto a silicon substrate.

the fabrication costs of the thick deposited films and to the low electrochemical performance attributed to the long transport path in the cross-plane direction of thick membranes.

A “design accepting buckling” is highly important for the fabrication of thin films in many applications where a stress-based failure is adopted. Although the important contribution from Ref. [9] toward a design in post-buckling regime, the application of the energy method in such a work is restricted to the axis-symmetry describing the first buckling where the secondary buckling (second bifurcation) is not captured and then excluded from the design space.

Important simulation results on the buckling of membrane in μ SOFC are shown in Refs. [10], however, there is always a need to provide a guideline for membrane designs based on both simulation results and experiments where fabrication and operation constraints in fuel cells are considered.

In the presented study, an advanced exploitation of the energy method is contributed to provide the needed informations on thin-film design in different buckling stages. The numerical results are

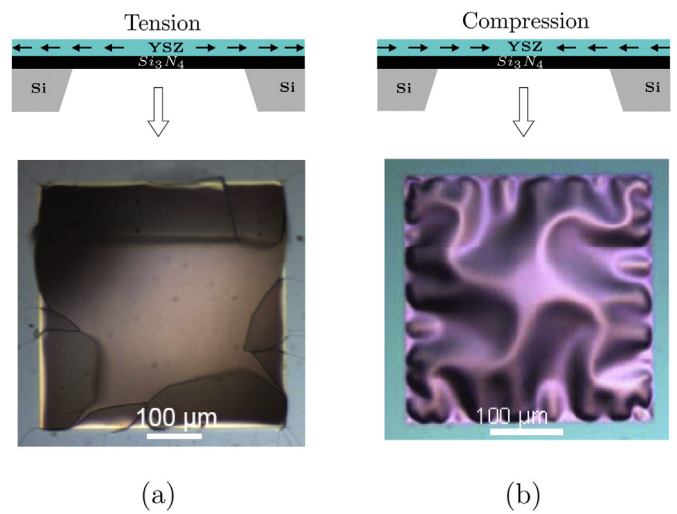


Fig. 3. Two typical results of free-standing YSZ membrane obtained from pulsed laser deposition. (a): YSZ membrane rupture after YSZ deposition at room temperature and annealing up to 400 °C at $3\text{ }^{\circ}\text{C min}^{-1}$. (b): membrane buckling after PLD deposition at 700 °C. Images are taken at room temperature.

experimentally validated in order to present a usable design space for YSZ electrolyte fabrication when the material properties are given and the residual stresses are evaluated depending on the manufacturing conditions.

By considering both rupture and buckling, the design concept adopted in this work allows a safe and flexible choice between various options of deposition conditions and film dimensions. Knowing that multi-layer thin plate clamped onto a stiff substrate is a prototype model for several laminated devices, the design method applied here is exploitable in different microfabricated products using thin film materials such as in chemical sensors, piezoelectric techniques, purification devices.

2. Energy minimization method

When the total potential energy of the thin film increases under residual compressive stresses, the film may take a new equilibrium state by performing a buckling instability transition to a new stable configuration. Energy minimization method is an adequate numerical approach to represent the principle of minimum potential energy and to predict system stability. In this paper, the needed topics on the simulations method are shortly introduced.

2.1. The potential energy of the film

The elastic energy in the domain Ω of a thin film with clamped boundaries (Fig. 4) is given by

$$F = \frac{1}{2} \int_{\Omega} \sigma : \epsilon d\Omega. \quad (1)$$

Here σ is the stress tensor and ϵ denotes the strain tensor written as

$$\epsilon_{ij}(z) = \delta_{ij}\epsilon_0 + \epsilon_{ij}^m + \epsilon_{ij}^b(z), \quad (2)$$

whereby $i, j \in \{x, y\}$ stand for the in-plane compounds, Fig. 4. The scalar ϵ_0 is the average value of the residual strain, δ_{ij} is the Kronecker delta. The terms ϵ_{ij}^m are the compounds of the membrane strain. They describe the elongation/contraction deformation and the stretching by shearing deformation of the middle surface of the film when any bending resistance is excluded. A nonlinear formulation of membrane strain is used in this based on the von Karman plate model:

$$\epsilon_{ij}^m = \frac{1}{2} \left(\frac{\partial u_i}{\partial j} + \frac{\partial u_j}{\partial i} + \frac{\partial w}{\partial i} \frac{\partial w}{\partial j} \right), \quad (3)$$

whereas u_i and u_j stand for the in-plane displacements and w denotes the out-of-plane deflection i.e. $\mathbf{u} = (u_x, u_y, w)$.

The terms ϵ_{ij}^b in Eq. (2) represent the bending and the twisting deformation of the film and is given as linear function of the "z" coordinate (see Fig. 4):

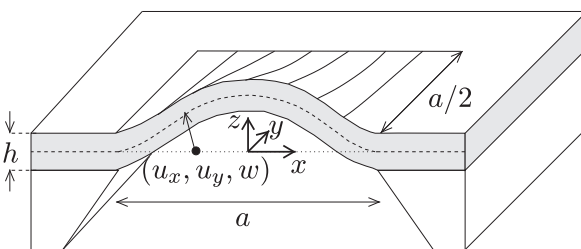


Fig. 4. Schematic representation of the buckling of a thin clamped film with side length a . The vector (u_x, u_y, w) denotes the displacement of a middle plane point.

$$\epsilon_{ij}^b(z) = -z \frac{\partial^2 w}{\partial i \partial j}. \quad (4)$$

Considering the case of plane stress model, the elastic energy F introduced in Eq. (1), can be subdivided into the membrane energy F_m and the bending energy F_b :

$$F = F_m + F_b. \quad (5)$$

Using the in-plane Hook's relations, we have the total membrane energy F_m of the film domain Ω :

$$F_m = \frac{Eh}{2(1-\nu^2)} \cdot \int_{-a/2}^{a/2} \int_{-a/2}^{a/2} \left(\epsilon_{xx}^2 + \epsilon_{yy}^2 + 2\nu \epsilon_{xx} \epsilon_{yy} \right)_{z=0} dx dy + \frac{Eh}{1+\nu} \int_{-a/2}^{a/2} \int_{-a/2}^{a/2} \epsilon_{xy}^2|_{z=0} dx dy. \quad (6)$$

The terms a and h denote the film side length and thickness respectively.

When clamped boundary conditions are considered, the sum of bending energy terms affected by the shear modulus, i.e. $E/2(1+\nu)$ (the second Lamé constant) vanish upon integration (this includes, however, the "twist" energy). Hence, the remaining bending energy of the film is written as:

$$F_b = \frac{Eh^3}{24(1-\nu^2)} \cdot \int_{-a/2}^{a/2} \int_{-a/2}^{a/2} \left(\frac{\partial^2 w}{\partial x^2} + \frac{\partial^2 w}{\partial y^2} \right)^2 dx dy. \quad (7)$$

The numerical solving of the buckling problem consists of two steps: firstly, Rayleigh–Ritz parameterization is applied in order to represent the displacement fields as summations of trial functions weighted by unknown coefficients (amplitudes). Secondly, a numerical minimization procedure is applied in order to determine the unknown coefficients to describe the film configuration in the stable equilibrium state.

2.2. Rayleigh–Ritz parameterization

The parameterization is split into two summation modes: a mirror-symmetric and an anti-mirror symmetric modes with respect to oxz and oyz planes with terms denoted by the superscripts "s" and "a" respectively. The in-plane displacement along x -direction is formulated as:

$$u_x(x, y) = \sum_{i,j=1}^p u_{ij}^s f_{ij}^s(x, y) + \sum_{i,j=1}^p u_{ij}^a f_{ij}^a(y, x), \quad (8)$$

where f_{ij}^s and $f_{ij}^a(x, y) = f_{ij}^s(y, x)$ are the trial functions affected by the unknown coefficients u_{ij}^s and u_{ij}^a , respectively:

$$f_{ij}^s(x, y) = \sin \frac{2i\pi x}{a} \cos \frac{(2j-1)\pi y}{a}. \quad (9)$$

The in-plane displacement in y -direction is written as

$$u_y(x, y) = u_x(y, -x). \quad (10)$$

The out-of-plane deflection is parameterized as superposition of buckle functions g_{ij}^s and g_{ij}^a affected by the unknown amplitudes w_{ij}^s and w_{ij}^a :

$$w(x, y) = \sum_{i=1, j=i}^m w_{ij}^s g_{ij}^s(x, y) + \sum_{i=1, j=i+1}^m w_{ij}^a g_{ij}^a(x, y), \quad (11)$$

where

$$g_{ij}^s(x, y) = \left(\cos \frac{2i\pi x}{a} - (-1)^i \right) \left(\cos \frac{2j\pi y}{a} - (-1)^j \right) + \left(\cos \frac{2j\pi x}{a} - (-1)^j \right) \left(\cos \frac{2i\pi y}{a} - (-1)^i \right),$$

and

$$g_{ij}^a(x, y) = \left(\sin \frac{(2i+1)\pi x}{a} - (-1)^i \sin \frac{\pi x}{a} \right) \cdot \left(\sin \frac{(2j+1)\pi y}{a} - (-1)^j \sin \frac{\pi y}{a} \right) - \left(\sin \frac{(2j+1)\pi x}{a} - (-1)^j \sin \frac{\pi x}{a} \right) \cdot \left(\sin \frac{(2i+1)\pi y}{a} - (-1)^i \sin \frac{\pi y}{a} \right).$$

It is observed that in-plane and out-of-plane trial functions satisfy the fixed boundary conditions of clamped film.

2.3. First and second buckling

Using the vector \vec{U} of the in-plane coefficients $\{u_{ij}^s\}_{i,j=1}^p \cup \{u_{ij}^a\}_{i,j=1}^p$ and the vector \vec{W} of out-of-plane amplitudes $\{w_{ij}^s\}_{i=1,j=i}^m \cup \{w_{ij}^a\}_{i=1,j=i+1}^m$, the potential energy in Eq. (1) is reintroduced here as a differentiable function of the vector \vec{U} , the vector \vec{W} , and, the scalar $\varepsilon_0 \in \mathbb{R}$ of residual strain:

$$F : \mathbb{R}^{2p^2} \times \mathbb{R}^{m^2} \times \mathbb{R} \longrightarrow \mathbb{R}$$

$$(\vec{U}, \vec{W}, \varepsilon_0) \rightarrow F(\vec{U}, \vec{W}, \varepsilon_0).$$

At equilibrium state, the minimum potential energy implies an in-plane stationary condition:

$$\frac{\partial F}{\partial \vec{U}} = \vec{0}. \quad (12)$$

The in-plane displacement is then obtained from Eq. (12) as nonlinear function of the out-of-plane deflection, this is denoted by the relation $\vec{U} = G(\vec{W})$.

The values of the coefficients w_{ij}^s and w_{ij}^a (compounds of \vec{W}) are obtainable by applying a minimization procedure (conjugate gradient) on the potential energy function $\tilde{F}(\vec{W}, \varepsilon_0) = F(G(\vec{W}), \vec{W}, \varepsilon_0)$.

For a given residual strain ε_0 , the stability of the system is controlled according to the Hessian matrix providing the double derivative of the energy function with respect to deflection amplitudes w_{ij}^s and w_{ij}^a . At the equilibrium point $(\vec{W}_e, \varepsilon_0)$, the Hessian matrix of order m^2 is obtained as

$$\mathcal{H}(\vec{W}_e, \varepsilon_0) = \frac{\partial^2 \tilde{F}(\vec{W}, \varepsilon_0)}{\partial \vec{W}^2} \Big|_{\vec{W} = \vec{W}_e}. \quad (13)$$

Let us consider the fundamental path of trivial solution $\vec{W}_e = \vec{0}$ which is denoted as FP1 in Fig. 5 and represents the state of unbuckled film. The onset of the first unstable equilibrium (primary buckling) is attributed to a threshold value of reduced compressive strain $\varepsilon_0 = \varepsilon_0^{c_1} < 0$ when the minimum eigenvalue of

$\mathcal{H}(\vec{0}, \varepsilon_0)$ denoted by $\lambda^{c_1} = \lambda_{\min} = \min\{\lambda_i\}_{i=1}^{m^2}$ vanishes. Within a range of high in-plane compressive values where $\varepsilon_0 < \varepsilon_0^{c_1} < 0$, there is a reduced residual strain $\varepsilon_0^{c_2} < \varepsilon_0^{c_1}$, for which the Hessian matrix \mathcal{H} at the equilibrium point $(\varepsilon_0^{c_2}, \vec{W}_e = \vec{0})$ has a multiple eigenvalue $\lambda^{c_2} = 0$. The strain beyond this critical value ($\varepsilon_0 < \varepsilon_0^{c_2}$) allows the clamped film to buckle either into the path of primary buckling with symmetric mode or into the path of secondary buckling with symmetry-breaking mode denoted BP2 in Fig. 5.

A double buckling point has been reported in several cases, see e.g. Refs. [11], and is associated with an eigenvalue multiplicity. In Ref. [12] a method for the prediction of second buckling is introduced in combination with application of the finite element method.

However, within the presented energy approach, the buckling transition of the square film can be iteratively controlled with respect to either dimensional or loading condition conditions. As example, let us consider the case of a film of Poisson ratio of $\nu = 0.20$ (value as that in e.g. Refs. [13], [14] and [15]) and thickness $h = 300$ nm subjected to a residual compressive strain $\varepsilon_0 = -0.002$. The simulations were performed by using Ritz expansions of degree $m = 4$ and $p = 5$. For a long side length a , this film can be in a stable secondary buckling mode represented by the path PB2 in Fig. 5 where the eigenvalues of the Hessian matrix $\mathcal{H}(\vec{W}_e, \varepsilon_0)$, Eq. (13), are strictly positive i.e. $\lambda_{\min} > 0$. Such a secondary buckling mode was iteratively predicted to take place for $a \geq a^{c_2} = 97$ μm , actually, the $\det \mathcal{H}(\vec{W}_e, \varepsilon_0)$ vanishes by an iterative decreasing the value of the film side length a toward a^{c_2} on the path PB2. On the other

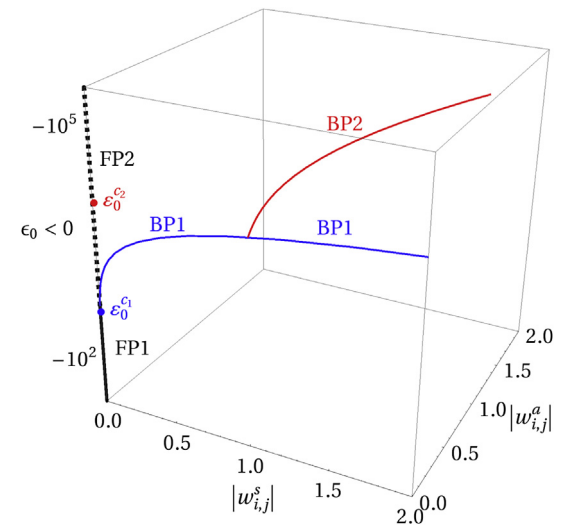


Fig. 5. Schematic of bifurcation of the equilibrium solution: $(\vec{W}_e, \varepsilon_0)$. FP1: fundamental path of a stable unbuckled state ($\varepsilon_0 > \varepsilon_0^{c_1}$, $w_{ij}^s = w_{ij}^a = 0$). BP2: fundamental path of an unstable unbuckled state ($\varepsilon_0 < \varepsilon_0^{c_1}$, $w_{ij}^s = w_{ij}^a = 0$). BP1: primary bifurcation path with axis symmetry shape ($\varepsilon_0 < \varepsilon_0^{c_1}$, $w_{ij}^s \neq 0$, $w_{ij}^a = 0$). BP2: secondary bifurcation path with symmetry breaking shape ($\varepsilon_0 < \varepsilon_0^{c_2}$, $w_{ij}^s \neq 0$, $w_{ij}^a \neq 0$).

hand, the first buckling was investigated using the condition $\det \mathcal{H}(\vec{0} = 0, \varepsilon)$ on the path FP1 in Fig. 5, it was predicted to be taking place at $a \geq a^{c_1} = 12.8 \mu\text{m}$.

3. Film in different buckling stages

The results shown in Fig. 6 are obtained by performing simulation tests with high degree of Ritz expansion: $m = 10$ and $p = 20$ where the buckling load for $\nu = 0.20$ and $E = 200 \text{ GPa}$ is $\sigma_0^{c_1} = -0.538 \text{ MPa}$.

The first buckling mode is shown in Fig. 6(a) for a residual compressive stress $\sigma_0 = -12.5 \text{ MPa}$. A film in this primary buckling stage allows a minimization of the total stored potential energy by an exchange from membrane energy to bending energy.

Note that the secondary buckling load is predicted as $\sigma_0^{c_2} = -30.9 \text{ MPa}$. The deformations in Fig. 6 (b and c) represent an advanced stage of secondary buckling under compressive residual stresses: $\sigma_0 = -125$ and -325 MPa respectively. The film's shape in this secondary mode is characterized by the symmetry breaking associated with a new mode of energy storage: a certain amount of membrane energy is released by elongation deformation, another amount is transferred to bending energy and a considerable amount of membrane energy is stored as a membrane shear energy. Hence, to absorb more energy in bending form, the thin film should have more local curvature and this justifies the observed branched folds and wrinkling at the boundaries. The folds in Fig. 6(c) are more twisted compared to Fig. 6(b) and this is associated with a higher amount of stored membrane shear energy. See Appendix A.

The above mentioned Young's modulus was obtained based on nanoindentation measurements performed on an 8YSZ film of thickness of $h = 300 \text{ nm}$ deposited by pulsed laser deposition at $700 \text{ }^\circ\text{C}$. The influences of the variation of the value of the Young's modulus on the buckling analysis can be discussed in the sense of both deflection magnitude, and instability transition. Considering a film with a defined ratio of thickness-to-side-length (h/a), a given Poisson's ratio (ν), and exposed to a constant residual compressive stress (σ_0):

- i Within a given buckling mode, a changing of the Young's modulus values should affect the magnitude of the out-of-plane deflection: an increased/decreased value of Young's modulus should effectively result in a lower/higher buckling amplitude.
- ii If the film is exposed to the residual compressive values (σ_0) such that, the mechanical equilibrium of the system is found to be in the neighboring of the buckling transition (around the point of an unstable equilibrium state), a perturbation of the value of the Young's modulus may shift the threshold value of the buckling loads ($\sigma_0^{c_1}$ or $\sigma_0^{c_2}$) and then the film may be found within another mechanical equilibrium, i.e. it may perform a transition between unbuckled state, primary or secondary buckling mode.

On the other hand, if the film was exposed to a constant residual compressive strain (not stress) the variation of the Young's modulus should affect only the buckling amplitude without changing the buckling mode.

4. Experimental validation

We shall recall that for a relevant comparison of simulation results to experimental measurements it is important to insure the accuracy of the used input data.

For this purpose, a consistent procedure is introduced here in order to extract the effective value of residual stresses in the YSZ film from the experiments.

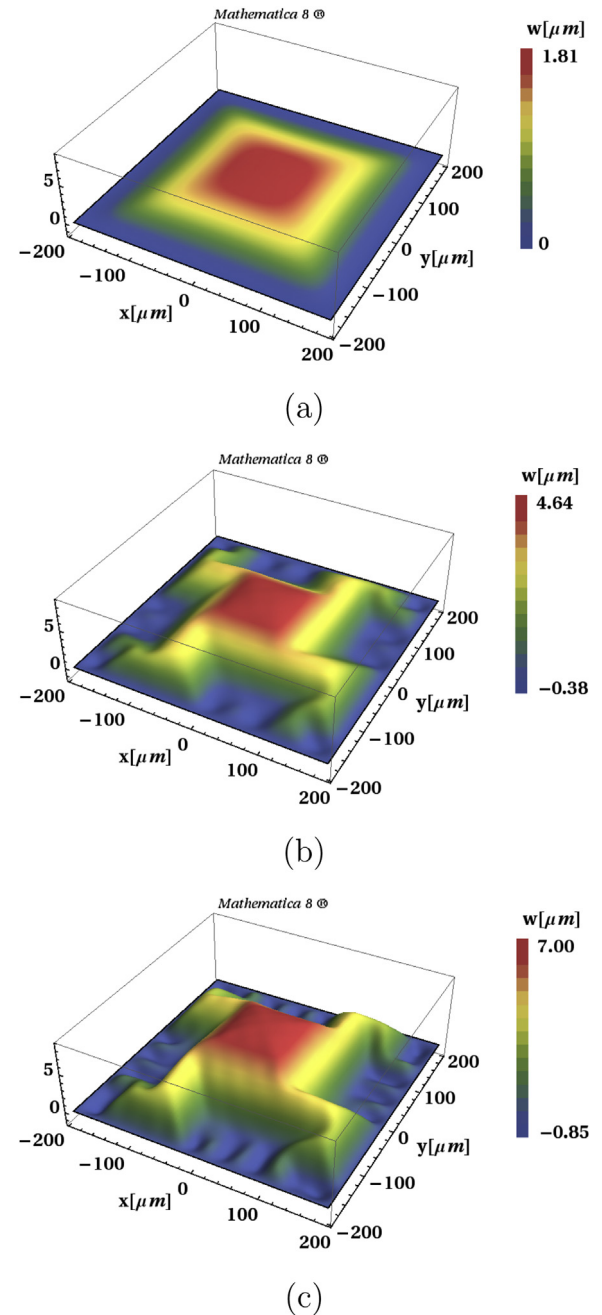


Fig. 6. (a) First buckling with axis symmetry for $\sigma_0 = -12.5 \text{ MPa}$. (b) and (c) Second buckling with rotational symmetry for $\sigma_0 = -125$ and -325 MPa respectively. Ritz degrees: $m = 10$ and $p = 20$.

4.1. A sequence of curvature measurements of multi-layers sample without etching

The residual stress in the multi-layers domain is estimated from the knowledge of the wafer curvature by applying of Stoney formula (see Ref. [16]). The curvature is evaluated at room temperature based on the optical measurements sequentially applied on the sample at different coating steps depicted in Fig. 7:

Firstly, the curvature measurements were applied on a top side coated silicon substrate and then on a double side coated substrate. From the difference between (a) and (b) curvature measurements, a tensile stress $\sigma_{\text{SNS}}^t = 128 \text{ MPa}$ is estimated in the silicon nitride membrane. The stress in the YSZ layer was determined by taking

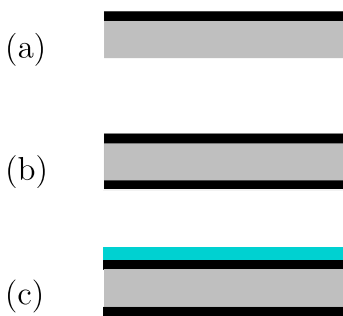


Fig. 7. Optical measurement of curvature is performed at each step of sample preparation: (a) Silicon wafer 380 μm thick is top side coated with 200 nm Si_3N_4 . (b) Wafer is double side coated with 200 nm Si_3N_4 . (c) Sample is top side coated with 300 nm YSZ film.

difference between (b) and (c) curvature measurements when this film is found to be storing a residual compressive stress of $\sigma_f^c = -1350$ MPa.

4.2. Effective residual stress in free-standing YSZ film

It is worth to note that residual stress obtained from the aforementioned measurements does not represent the effective value of the stresses when the film is deposited on an etched substrate. The etching of an underlying silicon substrate allows more compliance in the structure since the total thickness has been extremely reduced by the factor $(h_1 + h_2)/(h_1 + 2h_2 + h_3) < 1/500$. Therefore, the stiffness of the free-standing (post-etching) double-layer is extremely lower than the total stiffness of the substrate-film sample, Fig. 8. This reduces an important amount of the residual stress especially that deformational effects arise early in the structure (even before buckling) during the film's deposition on the thin (etched) substrate.

Further, it is not practical to measure the pre-buckling residual compressive stress in a film deposited on an etched substrate since we take out the film already buckled from the deposition machine.

For an experimental validation, it is instructive to establish a method for an accurate estimation of the residual stress in the free-standing membrane deposited on an etched substrate.

In such a perspective, the stress analysis of the curvature measurements in Fig. 7 is applied to predict the misfit strain between YSZ and Si_3N_4 layers in substrate-supported film case. Therefore, within the feature of free-standing membrane, a stress analysis of the YSZ- Si_3N_4 double layer is reperformed by using the aforementioned misfit strain as interface condition and finally, the compressive stress in the free-standing YSZ film is obtained as an explicit function of the measured stresses σ_f^c and σ_{SNS}^t , see Appendix B and Appendix C, mainly Eq. (C.7):

$$\sigma_{\text{YSZ}} = \frac{\left(\frac{B_2}{B_1} - 4\frac{h_1}{h_s}\right)\sigma_f^c - \sigma_{\text{SNS}}^t}{\frac{h_1}{h_2} + \frac{B_2}{B_1} + \frac{3h_1(h_1+h_2)^2B_2}{h_1^2B_1 + h_2^2B_2}}. \quad (14)$$



Substrate-supported YSZ film

Here $h_1 = 300$ nm is the YSZ film thickness and $h_s = 2h_2 + h_3$ is the substrate thickness with $h_2 = 200$ nm and $h_3 = 380$ μm are the Si_3N_4 film coating thickness and the wafer Si thickness respectively (see Fig. 8), the terms $B_i = E_i/1 - \nu_i$, $i = 1, 2$, are the biaxial modulus of YSZ and Si_3N_4 film respectively. The Young's modulus of the YSZ film $E = 200$ GPa is obtained by using nanoindentation measurements where the Poisson ratio is $\nu_1 = 0.20$. The total thickness of the double side coated substrate $h_s = 2h_2 + h_3 = 380.4$ μm . The residual stress obtained from curvature measurements in substrate-supported film feature are $\sigma_f^c = -1350$ MPa for YSZ film and $\sigma_{\text{SNS}}^t = 128$ MPa in the Si_3N_4 film. The biaxial modulus of the silicon nitride is considered as $B_2 = 385$ GPa. By substituting in Eq. (14), the effective value of compressive residual stress in the free-standing YSZ film is $\sigma_{\text{YSZ}} = -186$ MPa.

4.3. Effect of underlying Si_3N_4 layer on membrane buckling

In order to incorporate the effects of the underlying thin Si_3N_4 layer ($h_2 = 200$ nm) on the buckling of YSZ membrane, Fig. 8, a validated procedure is introduced based on:

- a. The driving force for the buckling is the residual compressive stress restricted to YSZ membrane.
- b. An underlying thin Si_3N_4 layer may affect the plate deformation by increasing the stiffness of the system.

Therefore, an equivalent buckling problem is considered as follows:

- i A plate domain is restricted to the clamped YSZ membrane of thickness h_1 subjected to a compressive residual stress σ_{YSZ} .
- ii Increased stiffness values equivalent to those of YSZ- Si_3N_4 double layers are assigned to the single YSZ layer.

Indeed, the prefactors of the integrals in the equations (5), (6) and (7) are $D = Eh^3/12(1 - \nu^2)$, $G_s = Eh/1 + \nu$ and $G_m = Eh/1 - \nu^2$ respectively. They represent the bending stiffness, the membrane shear stiffness and the elongation stiffness respectively, for a single layer. They are substituted by assigned values of average total stiffness for double-layer membrane:

- $D \leftarrow D\left(\frac{h_1+h_2}{h_1}\right)^2 \left[1 + \left(\frac{h_2(1-\nu_1^2)E_2}{h_1(1-\nu_2^2)E_1}\right)\right]$,
- $G_s \leftarrow G_s\left(1 + \frac{h_2(1+\nu_1)E_2}{h_1(1+\nu_2)E_1}\right)$,
- $G_m \leftarrow G_m\left(1 + \frac{h_2(1-\nu_1^2)E_2}{h_1(1-\nu_2^2)E_1}\right)$.

Note that the subscripts $i = 1, 2$ stand for YSZ and Si_3N_4 respectively. The above assigned values are obtainable considering the shear modulus and plane strain modulus as average values over the total thickness i.e. $\sum_{i=1}^2 \frac{h_i E_i}{2(h_1+h_2)(1+\nu_i)}$ and $\sum_{i=1}^2 \frac{h_i E_i}{(h_1+h_2)(1-\nu_i^2)}$.



Free-standing YSZ- Si_3N_4 membrane

Fig. 8. Residual stresses are strongly released in free-standing sample due to “etching-induced compliance” associated with an extreme decrease of total thickness by a factor $(h_1 + h_2)/(h_1 + 2h_2 + h_3) = 1/761.4$.

Simulations of the buckling of YSZ film were performed with both cases of single-layer values and assigned double-layers stiffness values. The effect of the underlying Si_3N_4 on the buckling results was found in agreement to the prediction contributed elsewhere using another approach of averaging residual strain in bi-layer, see Refs. [12], page 111. Moreover, it is stated experimentally, that reactive ionic etching of the thin underlying Si_3N_4 (see Fig. 1 (e)) was applied without observing considerable change in the buckled film configuration. Consequently, the deformation of the double-layer was mainly driven (dominated) by the buckling of the YSZ membrane.

4.4. Optical profilometry measurements

The 300 nm thick YSZ membrane was deposited by using PLD at 700 °C onto a free-standing layer of 390 μm side length. This membrane is found to have a buckled shape and deformation is measured at room temperature by using an optical profilometry technique (Wyko NT100 white light interferometer). The buckling shape and amplitude is detected with high accuracy and illustrated in 3D view in Fig. 9(a) where the secondary buckling mode is clearly observed. The measured amplitude at the center of the buckled membrane is $W_{\max} = 5.74 \mu\text{m}$.

On the other hand, numerical simulation is performed for a residual compression σ_0 based on the aforementioned analysis of curvature measurements i.e. $\sigma_0 = \sigma_{\text{YSZ}} = -186 \text{ MPa}$. By choosing a degree of Rayleigh–Ritz expansion with $m = 10$ and $p = 20$, the use of in-plane equilibrium conditions reduce the degree of freedom of

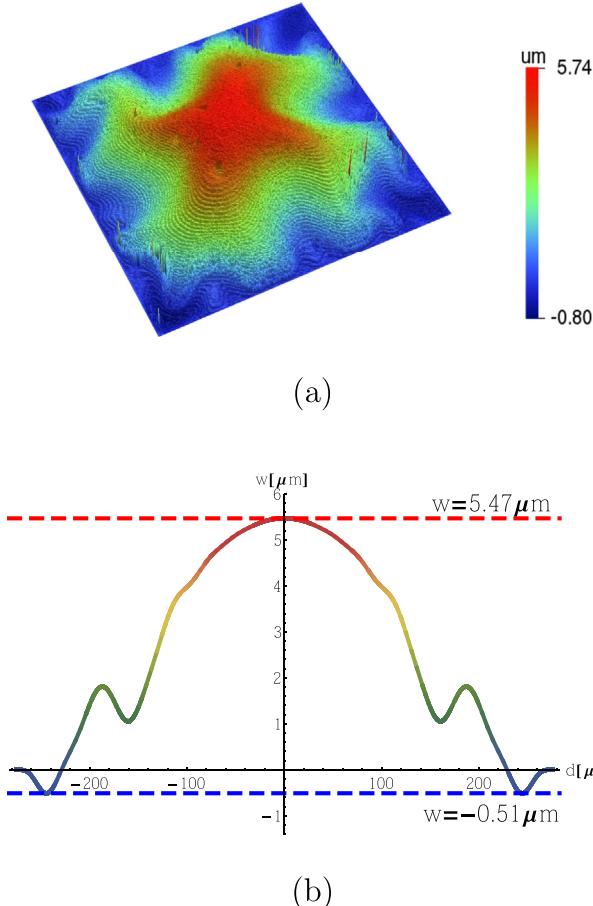


Fig. 9. (a) 3D view of a buckled 300 nm thick YSZ membrane taken with white light interferometry shows an “octopus”-like pattern with folded boundaries. (b) Simulation results showing the deflection values along the diagonal direction of the buckled film (in-house Mathematica code is used).

Table 1

Buckling amplitudes obtained from simulations are compared with the optical measurements. Deviations (ΔW) are given relatively to the maximum measured deflection $W_{\max} = 5.74 \mu\text{m}$.

	Model [μm]	Measured [μm]	$\frac{ \Delta W }{W_{\max}}$
Upward	5.47	5.74	4.7%
Downward	-0.51	-0.8	5%

the problem to $m^2 = 100$. The simulation results in Fig. 9(b) presents a buckling amplitude in good agreement with the measured amplitude value of buckled pattern shown in Fig. 9(a) (see Table 1).

The profile of the measured sample deviates slightly from the assumed rotational-symmetry and this reflects a local imperfection in the buckling behavior of the pattern related to uncontrollable material and geometrical effects during sample fabrication.

5. A guideline for design space

For a reliable structural design, it is important to define the failure mode and to establish the safety assessment with respect to the suitable yielding criterion. The maximum stress criterion (principal stress or Rankine criterion) states that failure occurs at a point in brittle material when a principal stress (σ_I or σ_{II}) reaches either the uniaxial tension strength $\sigma_t > 0$, or the uniaxial compression strength $\sigma_c < 0$.

However, a more conservative prediction, Coulomb–Mohr criterion, is often used to predict failure in brittle materials especially for plane stress problem:

$$\frac{(\max\{\sigma_I, \sigma_{II}\})^+}{\sigma_t} + \frac{(\min\{\sigma_I, \sigma_{II}\})^-}{\sigma_c} \geq 1. \quad (15)$$

Here, $(.)^+/(.)^-$ is the positive/negative part notation (it vanishes if $(.)$ is a negative/positive value, else, it is equal to $(.)$). Fig. 10 shows three buckling test cases simulated with a low order Ritz expansion $m = 4, p = 5$. Under compressive stress value $\sigma_0 = -300 \text{ MPa}$, it is observed that thin film with a short side length (70 μm) exhibits a primary buckling mode where the film of wide side length (150 μm and 500 μm) are in secondary buckling.

The film in primary buckling undergoes a high tensile stress in Fig. 10(b₁) near the boundaries where yielding are detected in Fig. 10(d₁) for mechanical strengths $\sigma_t = 250 \text{ MPa}$ (value as that in e.g. Refs. [23] and [19]) and $\sigma_c = -1500 \text{ MPa}$. On the other hand, yielding is restricted to limited zones of high tensile stress in secondary buckling, see Fig. 10(b₂), (d₂). Moreover with a film of 500 μm side length we observe more stress relaxation within an advanced stage of secondary buckling where the film is fully safe.

The stress relaxation in post-buckling stage is investigated in Fig. 11 for the same aforementioned Ritz degrees and material properties. The extremum stresses are plotted against different values of side length a . It is observed that stresses are relaxed beyond a safety threshold value of $a = 180 \mu\text{m}$.

This simulation has been reproduced with different values of residual stresses and a least square method has been applied to formulate the dependency between residual stresses and safety lengths. Subsequently, a design space is formulated with respect to the geometrical and the material properties of the film and shown in Fig. 12. The yielding regions above the tensile strength and below compressive strength are excluded from safety-design area. In the remaining part, three safety regions are located: S_4 which is the unbuckled region and is located above the primary buckling curve which is a region of low stress and represents the classical conservative area of buckling-based failure design. The other regions, S_1 and S_2 , are located above the curves c_1 and c_2 in post-buckling regions where the stresses are controlled under the tensile

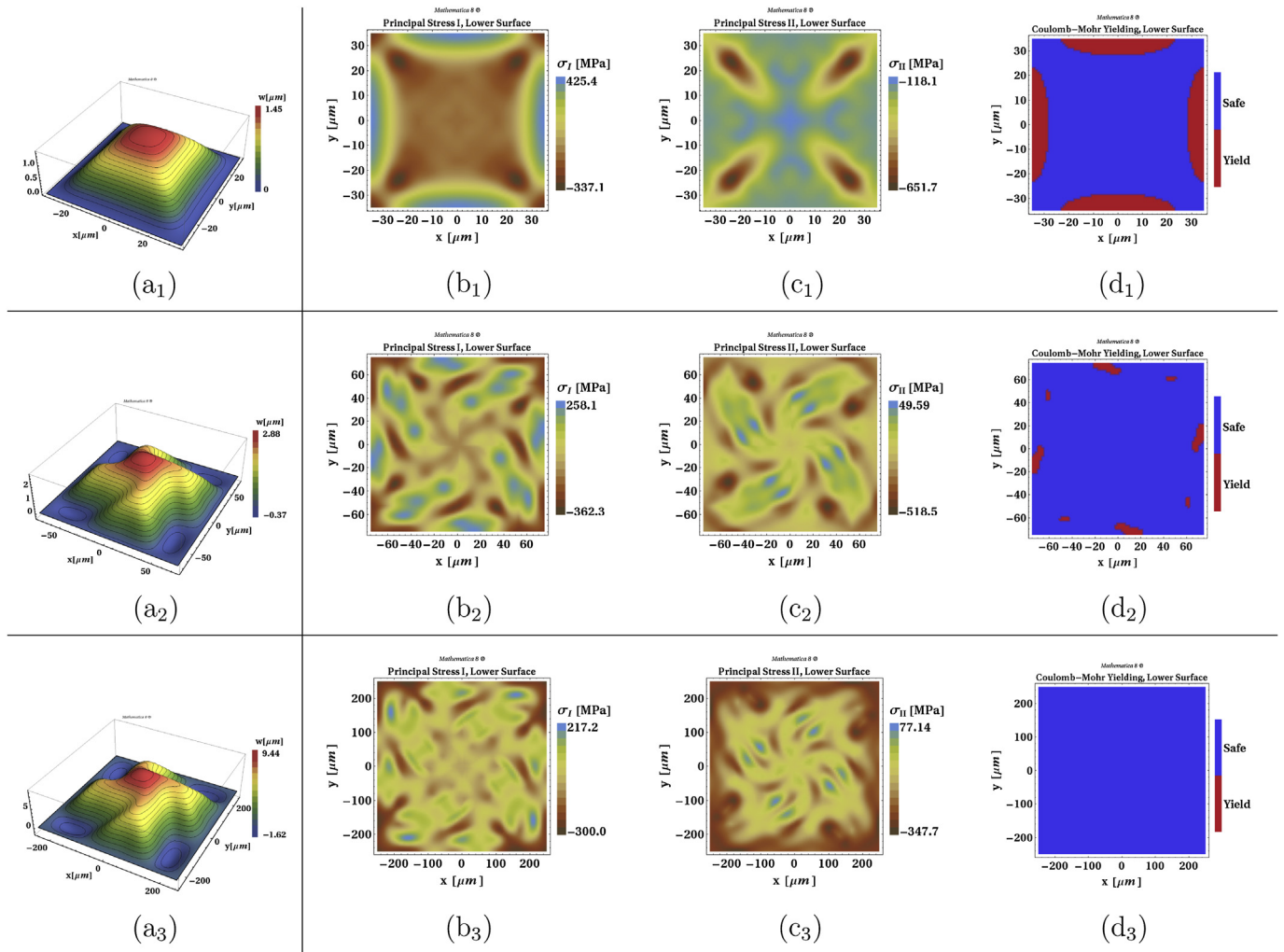


Fig. 10. Simulations are performed with Ritz degrees $m = 4$ and $p = 5$ on a film of thickness $h = 300$ nm for a residual stress $\sigma_0 = -300$ MPa. The subscripts $i \in \{1, 2, 3\}$ stand for films with side length 70 μm , 150 μm and 500 μm . (a_i) film buckling. Results are given on the lower surface denoted as (b_i) and (c_i) for principal stresses σ_I and σ_{II} and (d_i) for safety-yielding parts. $E = 240$ GPa, $\nu = 0.20$ and $\sigma_t = 250$ MPa.

strength $\sigma_t = 250$ MPa. The area of safe regions S_1 and S_2 are clearly larger than S_4 , therefore, the post-buckling analysis has allowed the prediction of a new wide design area.

It is worth to note that our experimental tests show a high survival rate of square 8YSZ films, (samples of 300 nm thickness

with different side-length values), in post-buckling regime when PLD deposition was performed at different temperatures 700 °C under 20 mTorr. All the samples that have survived the deposition were found in the predicted safe region of the derived design space shown in Fig. 12. More speaking, the safe fabricated buckled films of the ratios of side-length-to-thickness (a/h) were exposed to the effective compressive stresses values σ_0 obtained from the curvature measurements where the etching effects were accounted for through Eq. (14), (see Section 4.2, Appendix B and C) and the corresponding points $(a/h, \sigma_0)$, marked as \odot , were all found above the curves c_1 and c_2 limiting the safety regions in Fig. 12. Moreover, the 8YSZ samples deposited at 400 °C under 2 mTorr pressure were all cracked and actually found in the predicted unsafe region where the corresponding points $(a/h, \sigma_0)$ are marked as \otimes .

6. Conclusion

The buckling of YSZ thin-film membranes in μ SOFC is analyzed by applying the Rayleigh–Ritz approach. A posteriori analysis of the stress measurements is suggested to derive the effective residual stress in the free-standing membrane. The simulation results are found to be in agreement with the experimental measurements. The thin membrane electrolyte is shown to survive in an advanced stage of post-buckling and an extended area of safety region is

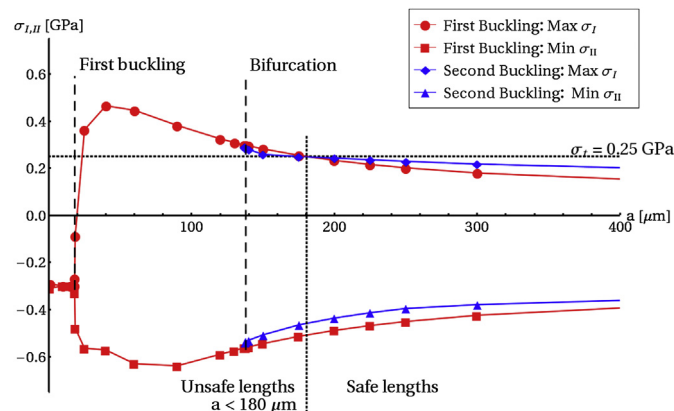


Fig. 11. Extremum values of principal stresses for a 300 nm thick film in first and second buckling stages under a residual stress $\sigma_0 = -300$ MPa. Safety lengths $a > 180$ μm are determined using Rankine criterion.

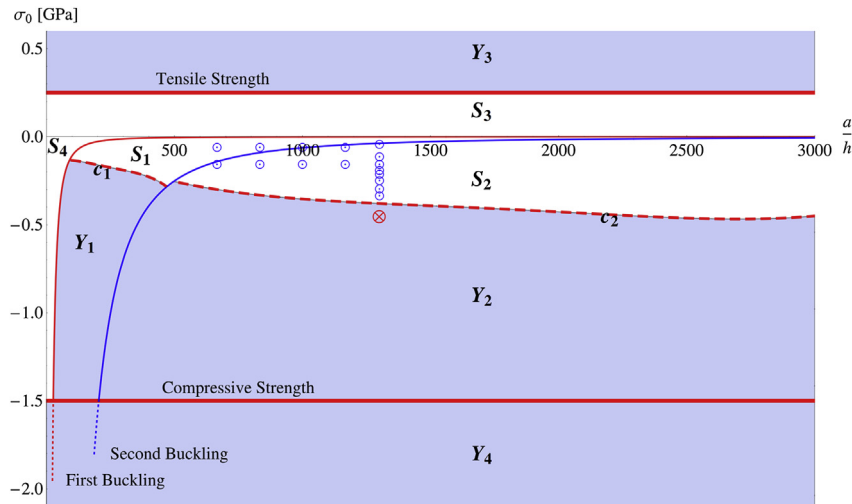


Fig. 12. A design space for thin film deposition. Safe regions are denoted as S_i where unsafe regions (regions to avoid from design) are denoted as Y_i , $i = 1, 2, 3, 4$. The curves c_1 and c_2 are the thresholds of controlled stresses in the primary and the secondary post-buckling regions. These curves are the delimiters of the safe zones S_1 and S_2 of controlled stresses where $\max\{\sigma_1, \sigma_2\} < \sigma_t$ and $\sigma_0 > \sigma_c$. The simulations are performed with Ritz expansion of degrees $m = 4$ and $p = 5$, for Young's modulus $E = 240$ GPa, Poisson ratio $\nu = 0.2$ and tensile strength $\sigma_t = 250$ MPa. All the 8YSZ samples (square films of 300 nm thickness with different side-length values) deposited at different temperatures under 20 mTorr pressure have survived the deposition and were found in the predicted safe region marked as \circ . The 8YSZ samples deposited at 400 °C under 2 mTorr pressure were all cracked and found in the predicted unsafe region marked as \otimes .

shown in a post-buckling design space. An advanced exploitation of the energy approach would be the prediction of post-buckling design space for different plate geometries (square, rectangular, circular) for an optimal design for YSZ manufacturing. This would be the topic of a future work. The method used in this work is usable as a step in the study of the effects of the integration of electrodes (that have a different thermal stress behavior) with the YSZ electrolyte. This would also be one of the topics of a new paper on the prediction of the safety of the multi-layers.

Acknowledgments

The authors are grateful for the fruitful collaboration with M.V.F. Schlupp, R. Tölke and A. Bieberle Hütter from the Nonmetallic Inorganic Materials group of Prof. L.J. Gauckler at the Swiss Federal Institute of Technology Zurich (ETHZ). The authors also would like to thank D. Courty from Nanometallurgy Laboratory at ETHZ for providing the nanoindentations measurements. A. Neels and O. Sereda from The Centre Suisse d'Électronique et de Microtechnique (CSEM), Neuchâtel are thanked for discussing stresses in thin films. D. Briand and J. Courbat from the group of N.F. de Rooji at SAMLAB Laboratory at École Polytechnique Fédérale de Lausanne (EPFL) are also acknowledged for providing the optical profilometry measurements, discussions and collaborations. Finally, this work is supported by the Swiss National Foundation under SNF, Sinergia contract #CRSI22-126830.

Appendix A. Energy storage modes

When the film is in an unbuckled shape for $\sigma_0 > \sigma_0^{c1} = -0.538$ MPa, the potential energy is stored exclusively as membrane energy which is “strongly increasing” as the in-plane residual compression is augmented in pre-buckling stage, see Fig. A.13(a). A film in primary buckling stage exhibits a “lower increase” of the potential energy. Indeed in Fig. A.13(a), it can be observed that the post-buckling potential energy curve has the slope of the tangent to the pre-buckling curve at the transition point of first buckling i.e. $\sigma_0 = \sigma_0^{c1} = -0.538$ MPa. Hence, buckling allows a more efficient minimization of the potential energy by

an exchange from membrane energy to bending energy. The membrane shear-energy storage is minor in the first buckling and this corresponds to the axis-symmetry shape of the buckled film. In secondary buckling, a different mode of energy storage is taking place with a considerable amount of membrane shear energy Fig. A.13(b), this can only be ensured by breaking the mirror symmetry of the deformation.

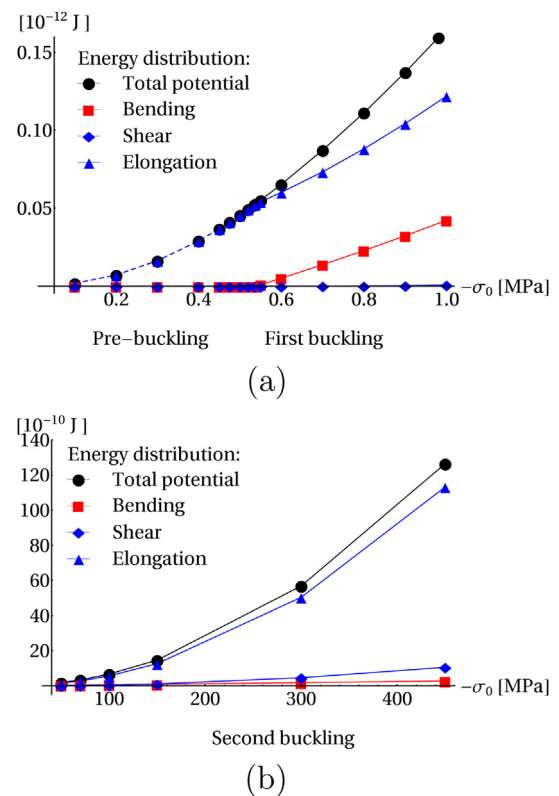


Figure A.13. Distribution of potential energy in different stages of loading σ_0 : (a) pre and first buckling and (b) second buckling. Ritz degree $m = 4$, $p = 5$.

Appendix B. Film-substrate misfit strain

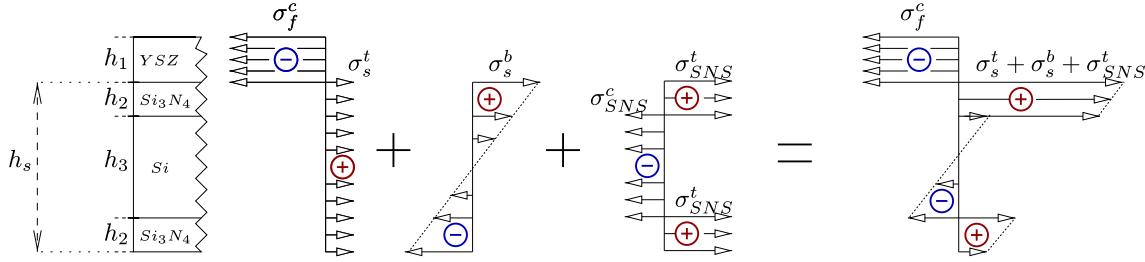


Figure B.14. A representation of stress distribution in the cross-section of the sample consisting of YSZ film deposited on substrate-supported silicon nitride film (a sample without etching).

In this appendix, the misfit strain at the interface between film and substrate is extracted from the curvature measurements in the case of the substrate-supported film. This estimation will be used in [Appendix C](#) as interface condition to obtain the effective residual stress in the case of free-standing membrane. The stress values in a case of substrate-supported film (without etching) is obtained by superposing the following stress contributions:

- The residual stresses in Si_3N_4 -Si- Si_3N_4 substrate, [Fig. 7\(b\)](#), which represent a misfit interaction between Si_3N_4 and Si material. From the curvature measurements (see [Fig. 7](#), steps (a) and (b)) we have $\sigma_{\text{SNS}}^t = 128$ MPa the tensile stress in the Si_3N_4 film. Since the system is not subjected to an external traction the force equilibrium yields a compressive stress in silicon wafer: $\sigma_{\text{SNS}}^c = -\frac{2h_2}{h_3}\sigma_{\text{SNS}}^t$.
- The stresses obtained from the curvature measurements (see [Fig. 7](#), steps (b) and (c)) which are compressive in YSZ film where $\sigma_{\text{f}}^c = -1350$ MPa and tensile in Si_3N_4 -Si- Si_3N_4 substrate (denoted by subscript "s"). Based on the force equilibrium we obtain

$$\sigma_s^t = -\frac{h_1}{h_s}\sigma_{\text{f}}^c, \quad (\text{B.1})$$

where h_1 is the YSZ film thickness and $h_s = 2h_2 + h_3$ is the substrate thickness with h_2 and h_3 are the Si_3N_4 film coating thickness and the wafer Si thickness respectively.

- The bending stress denoted by σ_s^b in Si_3N_4 -Si- Si_3N_4 , it is written as

$$\sigma_s^b(z) = \frac{-B_s}{R}z, \quad \forall z \in \left[-\frac{h_s}{2}, \frac{h_s}{2}\right], \quad (\text{B.2})$$

where R is the measured curvature radius and B_s is the average biaxial modulus of the substrate $B_s = 2B_2h_2 + B_3h_3/h_s$ whereas $B_i = E_i/1 - \nu_i$, $i = 2, 3$, are the biaxial modulus of Si_3N_4 film and Si wafer respectively. Further, Stoney's relation of film stress $\sigma_{\text{f}}^c = -\frac{h_s^2 B_s}{6R h_1}$ is substituted into Eq. (B.2) giving:

$$\sigma_s^b(z) = -6\frac{\sigma_{\text{f}}^c h_1}{h_s^2}z, \quad \forall z \in \left[-\frac{h_s}{2}, \frac{h_s}{2}\right]. \quad (\text{B.3})$$

The bending stress in the film is disregarded because of its low bending stiffness compared to the thick substrate. Now the misfit strain $\varepsilon_{\text{mis fit}}$ at the interface between YSZ and Si_3N_4 films where $z = h_s/2$ is obtain as:

$$\begin{aligned} \varepsilon_{\text{mis fit}} &= \frac{\sigma_{\text{f}}^c}{B_1} - \frac{\sigma_s^t + \sigma_s^b(h_s/2) + \sigma_{\text{SNS}}^t}{B_2} \\ &= \left(\frac{1}{B_1} + \frac{4h_1}{h_s B_2}\right)\sigma_{\text{f}}^c - \frac{\sigma_{\text{SNS}}^t}{B_2}, \end{aligned} \quad (\text{B.4})$$

where B_1 denotes the biaxial modulus of YSZ supported film.

Appendix C. Residual compressive stress in the free-standing YSZ film

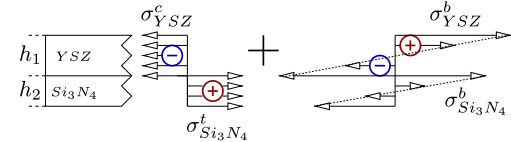


Figure C.15. A representation of stress in the free-standing YSZ and Si_3N_4 membranes.

Considering the free-standing YSZ- Si_3N_4 double layer, see [Fig. 8](#), in an unbuckled state (this corresponds, however, to either a stable pre-buckling state under low in-plane compressions, $\varepsilon_0 > \varepsilon_0^{\text{c1}}$, or to an assumed unstable equilibrium state of unbuckled film under high in-plane compressions, $\varepsilon_0 < \varepsilon_0^{\text{c1}}$, see the paths FP1 and FP2 in [Fig. 5](#)).

The interaction between the two layers is effected by the forces and the moment acting at the interface. Similar to the approach introduced by Refs. [17], and used later by Refs. [18], [19] and [20], in this work each layer is modeled as a beam and the aforementioned interface forces and moment are converted to equivalent stress (or force) and moment system referred to the centroidal axis of each layer. The bending stresses are:

$$\sigma_{\text{YSZ}}^b(z) = \frac{B_1}{R_{\text{fs}}}z, \quad \forall z \in \left[-\frac{h_1}{2}, \frac{h_1}{2}\right], \quad (\text{C.1})$$

$$\sigma_{\text{Si}_3\text{N}_4}^b(z) = \frac{B_2}{R_{\text{fs}}}z, \quad \forall z \in \left[-\frac{h_2}{2}, \frac{h_2}{2}\right], \quad (\text{C.2})$$

where a plate curvature of radius R_{fs} (free-standing curvature radius) is assumed.

The residual compressive stress in YSZ membrane (denoted here as σ_{YSZ}^c) cannot be estimated from the classical Stoney's formula since the condition of thick substrate ($h_2 \gg h_1$) is not satisfied. Considering the torque freedom condition at the middle plane of Si_3N_4 layer ([Fig. C.15](#)), the moment equilibrium is written as:

$$\begin{aligned} & \int_{-h_1/2}^{h_1/2} \sigma_{YSZ}^c \frac{h_1 + h_2}{2} dz + \int_{-h_1/2}^{h_1/2} \sigma_{YSZ}^b(z) \left(z + \frac{h_1 + h_2}{2} \right) dz \\ & + \int_{-h_2/2}^{h_2/2} \sigma_{Si_3N_4}^b(z) dz = 0. \end{aligned} \quad (C.3)$$

Substituting for σ_{YSZ}^b and $\sigma_{Si_3N_4}^b$ from Eqs (C.1, C.2) into Eq. (C.3), a new formulation (generalization) of Stoney's relation is obtained as (Stoney–Safa):

$$\sigma_{YSZ}^c = -\frac{h_1^3 B_1 + h_2^3 B_2}{6R_{fs} h_1 (h_1 + h_2)}. \quad (C.4)$$

For a very thin film ($h_1 \ll h_2$), this equation gives the classical Stoney's formula. The tensile stress in the Si_3N_4 membrane is obtained from force equilibrium conditions:

$$\sigma_{Si_3N_4}^t = -\frac{h_1}{h_2} \sigma_{YSZ}^c. \quad (C.5)$$

The misfit strain $\varepsilon_{\text{misfit}}$ at the interface between YSZ and Si_3N_4 is obtained as a function of the free-standing membrane (post-etching) curvature radius R_{fs} :

$$\begin{aligned} \varepsilon_{\text{misfit}} &= \frac{\sigma_{YSZ}^c + \sigma_{YSZ}^b(z)}{B_1} \left|_{z=-\frac{h_1}{2}} \right. - \frac{\sigma_{Si_3N_4}^t + \sigma_{Si_3N_4}^b(z)}{B_2} \left|_{z=\frac{h_2}{2}} \right. \\ &= \frac{1}{R_{fs}} \left(-\frac{h_1^3 B_1 + h_2^3 B_2}{6h_1(h_1+h_2)B_1} - \frac{h_1}{2} - \frac{h_1^3 B_1 + h_2^3 B_2}{6h_2(h_1+h_2)B_2} - \frac{h_2}{2} \right). \end{aligned} \quad (C.6)$$

This corresponds to the relation derived elsewhere see e.g. Refs. [21] and [22]. The misfit strain between the two membranes is etching-independent, and then, has the same value for both the substrate-supported film and free-standing membrane cases. Substituting for $\varepsilon_{\text{misfit}}$ from Eq. (C.6) into Eq. (B.4), we obtain an expression for the curvature radius R_{fs} of the free-standing membrane for an assumed unbuckled state.

Therefore, the compressive stress in the free-standing YSZ film is obtained by substituting the aforementioned obtained

expression for R_{fs} in Eq. (C.4). It is an explicit function of the measured stresses σ_f^c and σ_{SNS}^t :

$$\sigma_{YSZ}^c = \frac{\left(\frac{B_2}{B_1} - 4 \frac{h_1}{h_s} \right) \sigma_f^c - \sigma_{SNS}^t}{\frac{h_1}{h_2} + \frac{B_2}{B_1} + \frac{3h_1(h_1+h_2)^2 B_2}{h_1^3 B_1 + h_2^3 B_2}}. \quad (C.7)$$

References

- [1] R.M. Jones, Buckling of Bars, Plates and Shells, Bull Ridge Publishing, 2006.
- [2] F.N. Herman, IEEE Trans. Device Mater. Reliability 3 (4) (2003).
- [3] A. Evans, M. Prestat, R. Tölke, M.V.F. Schlupp, L.J. Gauckler, Y. Safa, T. Hocker, J. Courbat, D. Briand, N.F. de Rooij, D. Courty, Fuel Cells 12 (4) (2012) 614–623.
- [4] M. Prestat, Miniaturized free-standing SOFC membranes on silicon chips, in: 10th European SOFC Forum, 26–29 June, 2012, Lucerne Switzerland.
- [5] I. Garbayo, A. Tarancón, J. Santiso, A. Cavallaro, J. Roqueta, G. García, I. Gracia, C. Cane, N. Sabate, Fabrication and characterization of yttria-stabilized zirconia membranes for micro solid oxide fuel cells, in: Smart Sensors, Actuators, and MEMS IV Proc. of SPIE, 7362, 73621B SPIE, 2009.
- [6] Y. Kuru, S.R. Bishop, J.J. Kim, B. Yıldız, H.L. Tuller, Solid State Ionics 193 (2001), <http://dx.doi.org/10.1016/j.ssi.2011.04.012>.
- [7] H.L. Tuller, S.R. Bishop, Annu. Rev. Mater. Res. 41 (2001) 369–398.
- [8] Y. Tang, K.S. Jonathan, D.G. Wu, J.Z. Tang, J. Micromech. Microeng. 15 (2005) 185–192.
- [9] N. Yamamoto, D.J. Quinn, N. Wicks, J.L. Hertz, J. Cui, H.L. Tuller, B.L. Wardle, J. Micromech. Microeng. 20 (2010) 035027 (9pp).
- [10] K. Kerman, T. Tallinen, S. Ramanathan, L. Mahadevan, J. Power Sources 222 (2013) 359–366.
- [11] L. Bauer, H.B. Keller, E.L. Reiss, SIAM Rev. 17 (1) (1975) 101–122. Published by: Society for Industrial and Applied Mathematics.
- [12] V. Ziebart, Mechanical Properties of CMOS Thin Films, PhD thesis, Swiss Federal Institute of Technology, ETH Zurich, 1999.
- [13] C. Eberl, et al., J. Am. Ceram. Soc. 94 (2011) S120–S127.
- [14] S. Gadag, G. Subbarayan, J. Mater. Sci. 41 (2006) 1221–1232.
- [15] N. Yamamoto, Numerical Analysis of Strong Buckling Behavior of Square Thin Membranes Using ABAQUS, ES240 Project, December 14th, 2006, <http://imechanica.org/files/ES240Report.doc>.
- [16] G.G. Stoney, Proc. R. Soc. Lond. Ser. A 82 (1909) 172.
- [17] S. Timoshenko, J. Opt. Soc. Am. 11 (3) (1925) 233–255.
- [18] E. Suhir, J. Appl. Mech. Trans. ASME 53 (1986) 657–660.
- [19] J.W. Eischen, C. Chung, J.H. Kim, J. Electron. Packag. Trans. ASME 112 (1990) 16–23.
- [20] Z.Q. Jiang, Y. Huang, A. Chandra, J. Electron. Packag. 119 (1997) 127–132.
- [21] L.B. Freund, J.A. Floro, E. Chason, Appl. Phys. Lett. 47 (14) (1999) 1987–1989.
- [22] A.C. Klein, J. Appl. Phys. 88 (9) (2000) 5487–5489.
- [23] J. Kondoh, et al., J. Alloys Compd. 365 (2004) 253–258.